Nanoscale

PAPER

View Article Online
View Journal | View Issue

Cite this: *Nanoscale*, 2018, **10**, 15222

Uniform small-sized MoS_2 from novel solution-based microwave-assisted method with exceptional reversible lithium storage properties†

Xuehui Tian, Qiuming Gao, * Hang Zhang, Zeyu Li, Hong Xiao, Qiang Zhang and Li Ma

Received 9th April 2018,
Accepted 14th July 2018

DOI: 10.1039/c8nr02833h

rsc.li/nanoscale

Currently, MoS_2 is being investigated as a lithium-ion battery (LIB) anode material because of its high theoretical capacity. However, its significantly low electrochemical activity and cyclic stability limit its utilization. Nevertheless, small-sized MoS_2 possibly overcomes these issues. Herein, small-sized MoS_2 with uniform particle sizes of about 20–30 nm was prepared *via* a novel solution-based microwave-assisted precursor pyrolysis method. The resultant MW-MoS_2 sample has a high surface area of 96.9 $m^2\ g^{-1}$ and large pore volume (0.38 $cm^3\ g^{-1}$) with pore size distribution mainly in the meso/macropore scale, which are beneficial for electrolyte storage and low charge carrier conductive resistances. The large pore surface area and volume of the small-sized MoS_2 can also ease the volume expansion during the charging and discharging process. As an LIB anode, the MW-MoS_2 material exhibits an amazingly large specific capacity of 1355 mA h g^{-1} at a low current density of 0.5 A g^{-1}. At a high current density of 10 A g^{-1}, a specific capacity of 435 mA h g^{-1} is obtained, demonstrating its excellent rate capability. Furthermore, a large discharge capacity of 544 mA h g^{-1} is maintained after 500 cycles at 5 A g^{-1}, indicating its fascinatingly high cyclic stability.

1. Introduction

Lithium-ion batteries (LIBs) have been extensively researched for the various merits of high voltage, large capacity, low cost and environment-friendly characteristics.[1–3] However, there are still many problems that should be solved to meet the rapidly growing demands in electric vehicles and mobile electronics, which need a longer cyclic life and better rate performance. Because of its long cyclic life, low cost, and high structural stability during cycling,[4,5] graphite has been used as the commercial LIB anode material for many years. However, the theoretical capacity of graphite (372 mA h g^{-1}) is very low. Therefore, the search for high-performance LIB anode materials with a large capacity, high rate capability and desired lifetime is urgent.[1,6,7]

Two-dimensional (2D) graphene-like transition metal disulfides, a class of substances denoted as MS_2, where M is a Group-IV, -V or -VI transition metal,[8–11] have shown fascinating and remarkable properties, which have made them the focus of substantial research interest.[12–14] Molybdenum disulfide as a representative of the MS_2 family has been used in catalysis,[15] photothermal cancer therapy[16,17] and electrochemistry.[18,19] Recently, MoS_2 was investigated as an LIB anode material[20–22] due to its high theoretical capacity (670 mA h g^{-1}).[23,24] However, its significantly low electrochemical activity and cyclic stability limit its utilization in LIBs. Small-sized MoS_2 possibly overcomes these issues because of its increased contact area with electrolyte, which enhances the activity and decreases the transport distances of charge carriers, *i.e.*, electrons and/or electrolyte ions. Additionally, the large pore surface area and volume of small-sized MoS_2 may possibly ease the volume expansion during the charging and discharging process. Usually, MoS_2 with large particle sizes is obtained *via* traditional methods such as the solid-state method and hydrothermal technique. Even though routine solution-based methods may lead to a certain decrease in the MoS_2 particle size, the large particle size is still mainly caused by a long synthesis time.[3,25–29]

Microwave radiation is a fast, simple, uniform and energy efficient heating method. In the microwave heating process,

Key Laboratory of Bio-inspired Smart Interfacial Science and Technology of Ministry of Education, Beijing Key Laboratory of Bio-inspired Energy Materials and Devices, Beijing Advanced Innovation Center for Biomedical Engineering, School of Chemistry, Beihang University, Beijing 100191, P. R. China. E-mail: qmgao@buaa.edu.cn

†Electronic supplementary information (ESI) available: SEM and (HR)TEM images, XRD as well as N_2 sorption and pore size distribution of HT-MoS_2, TGA of MW-MoS_2, and rate capabilities and cyclic stabilities of the typical reported MoS_2 and MW-MoS_2. See DOI: 10.1039/c8nr02833h

the energy transfer between microwaves and the reaction substance or medium is accomplished by resonance-relaxation, which causes microwave heating to be fast and saves energy. Moreover, the heat is generated from inside the material rather than outside, which produces a small temperature gradient, making the heating more uniform.[30–32] In addition, microwaves can also change the spatial structure of some molecules, break some chemical bonds and activate molecules, thus promoting a variety of chemical reactions. Due to the superiority of the microwave method, herein, we present a novel solution-based microwave-assisted precursor pyrolysis method to prepare small-sized MoS_2 nanoparticles, which exhibit large reversible specific capacity, high rate capability and high cyclic stability.

2. Experimental section

All the chemicals were used without further purification. Ammonium molybdate tetrahydrate ($(NH_4)_6Mo_7O_{24}\cdot 4H_2O$, 81.0–83.0% MoO_3 basis), L-cysteine ($C_3H_7NO_2S$, 99%), and glycerol ($C_3H_8O_3$, 99%) were purchased from Beijing Chemical Works. Lithium metal foil, carbon black, polymer binder (polyvinylidene fluoride, PVDF), 2025-type coin cells, Celgard membrane and lithium hexafluorophosphate were purchased from Beijing HWRK Chem Co., Ltd.

The molybdenum disulfides were prepared, as shown in Scheme 1. Initially, 0.3 g of ammonium molybdate tetrahydrate and 30 mL of glycerol were mixed in a 100 mL beaker and stirred for 30 min. Also, 1.0 g of L-cysteine and 30 mL of glycerol were mixed in another 100 mL beaker and stirred for 30 min. Then, the liquids from these two beakers were mixed in a 250 mL three-necked flask and stirred for 60 min under argon atmosphere in an XH-200A Computer Microwave Solid–Liquid Phase Synthesis/Extraction Workstation to obtain a uniform suspension liquid. Following this, under vigorous stirring and argon atmosphere, the mixture was heated to 180 °C with microwave irradiation (800 W) for 5 min. This was followed by rapid cooling to room temperature. The as-synthesized intermediate precipitate was cleaned several times *via* centrifugation at 8500 rpm for 30 min with deionized water and ethanol. After the subsequent calcination at 800 °C for 2 h under argon atmosphere, the resultant MoS_2, named MW-MoS_2, was obtained. For comparison, the MoS_2 product named HT-MoS_2 was also prepared *via* the traditional hydrothermal method at 180 °C for 24 h using the same raw materials and subsequent calcination.

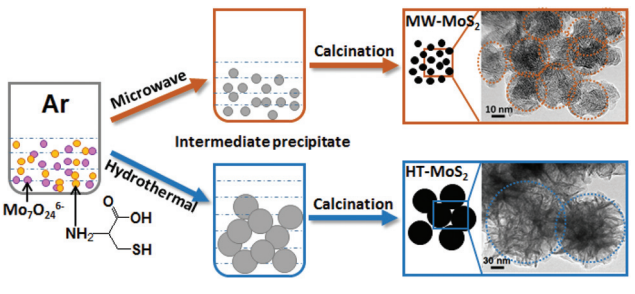

Scheme 1 The formation processes for the MW-MoS_2 and HT-MoS_2 samples.

The 2025-type coin cells were assembled in an argon-filled glovebox. The cathode slurry was prepared by mixing the active material (MoS_2), conductive agent (acetylene black) and binder (PVDF) with a weight ratio of 7 : 2 : 1 in *N*-methylpyrrolidone (NMP) solvent dispersant. The positive electrodes were prepared by pressing the slurry onto a copper foil current collector and drying at 60 °C for 12 h under vacuum. The half-cells were assembled using a porous membrane (Celgard 2400) as the separator and lithium metal as the counter electrode. The electrolyte was a $LiPF_6$ (1.0 M) solution in a mixture of ethylene carbonate/dimethyl carbonate (EC/DMC, 1 : 1 in volume).

The crystalline structure and phase purity of the samples were determined using powder X-ray diffractometry (XRD; LabX XRD-6000, Shimadzu, Japan) with Cu K_α radiation (λ = 1.5418 Å) at a scan rate of 6° min^{-1} in the range of 10° ≤ 2θ ≤ 80° at room temperature. The microstructures and morphologies of the samples were observed *via* field emission scanning electron microscopy (FE-SEM, JSM-7500), transmission electron microscopy (TEM, JEM-2100F) and high resolution TEM (HRTEM, JEM-2100F). The compositions of MW-MoS_2 were determined using energy dispersive X-ray spectroscopy (EDS, JSM-7500). The surface elemental compositions and microstructures were determined *via* X-ray photoelectron spectroscopy (XPS) using an Al K_α (150 W) monochromatic X-ray source (ESCALAB 250, Thermo Fisher Scientific, USA). Thermogravimetric analyses (TGA) were carried out under air atmosphere on an SDTQ600 (TA Instruments, USA) at a heating rate of 5 °C min^{-1} from room temperature to 700 °C. The Brunauer–Emmett–Teller (BET) surface areas were determined *via* N_2 adsorption and desorption isotherms at 77 K with an ASAP 2020 physisorption analyzer (USA).

The above assembled 2025-type coin-cell batteries were used for electrochemical performance testing. Galvanostatic charge–discharge measurements of the half-cells were tested using a multi-channel current static instrument LAND-CT2001A battery test system in the voltage range of 0.01–3.00 V *vs.* Li^+/Li. In the rate capability test, the charge and discharge current gradually increased from 0.5 to 10 A g^{-1}. To characterize the redox behaviour and the kinetic reversibility of the cell, cyclic voltammetry (CV) curves were obtained on a CHI660D electrochemical workstation with a scan rate of 0.2 mV s^{-1} between 0.01 and 3.00 V. Electrochemical impedance spectroscopy (EIS) curves were obtained using a CHI660D electrochemical workstation in the frequency range of 10 mHz to 100 kHz. All of the electrochemical tests were performed at room temperature.

3. Results and discussion

The particle size and morphology of the as-synthesized MW-MoS_2 were determined *via* SEM, and the images with different magnifications are presented in Fig. 1a and b. The

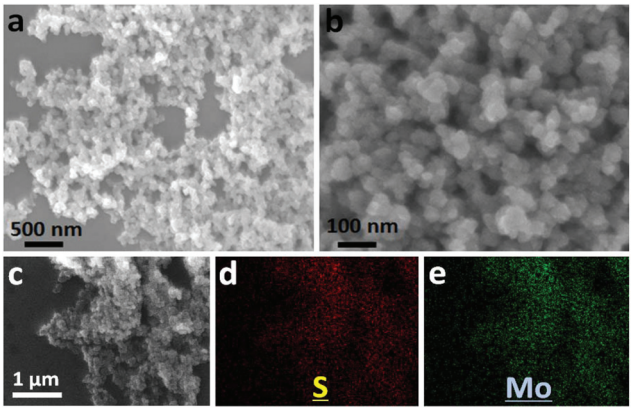

Fig. 1 (a, b) SEM images at different magnifications and (c) the SEM image and (d, e) its related elemental mapping of MW-MoS_2.

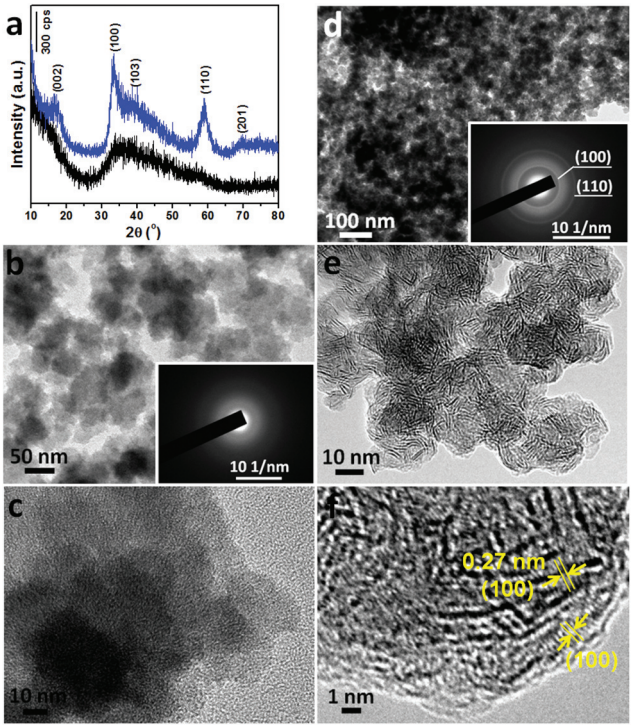

Fig. 2 (a) XRD patterns of the intermediate precipitate (black) and MW-MoS_2 (blue). (b, c) TEM images of the intermediate precipitate. (d, e) TEM and (f) HRTEM images of MW-MoS_2. The insets in (b) and (d) are the SAED patterns of the intermediate precipitate and MW-MoS_2, respectively.

particles of MW-MoS_2 are uniform and very small in size (about 20–30 nm) due to the very short reaction time (5 min) in the solution-based microwave radiation process. In contrast, the HT-MoS_2 has a large flower-like morphology and its particle size ranges from 200–500 nm (Fig. S1†). The EDS elemental mapping images (Fig. 1d and e) of MW-MoS_2 demonstrate that both Mo and S atoms are homogeneously distributed throughout the sample. The molar ratio of Mo/S is 0.5, which corresponds to the MoS_2 composition. Furthermore, TGA curve (Fig. S2†) analysis indicates that there is a weight loss of 9.9% at about 400 °C due to the decomposition of MoS_2, which was oxidized to MoO_3.[33,34]

In addition, the weight loss under 400 °C is due to the adsorbed moisture from the air since the small-size MW-MoS_2 has a large pore volume and BET surface area, which are described later. Also, the mass loss beyond 700 °C can be ascribed to the decomposition of MoO_3.[34]

The crystallinities of the as-prepared intermediate precipitate and MW-MoS_2 material were confirmed by XRD (Fig. 2a). The XRD pattern of the intermediate precipitate sample does not exhibit a (002) reflection peak, which is typically observed in its bulk analogue, indicating that the intermediate precipitate contains five or less 2D layered MoS_2.[35] After calcination, diffraction peaks at the 2θ values of 16.63°, 33.19°, 38.75°, 58.93° and 69.94° were observed, which correspond to the (002), (100), (103), (110) and (201) lattice planes of the hexagonal crystalline structure of MoS_2 (JCPDS 37-1492). No diffraction peaks from impurities or parasitic phases were observed.[33,36,37] The diffraction peaks of MW-MoS_2 are broad due to the small MoS_2 particle sizes, which will be beneficial for offering more active sites at the interface between the solid and liquid, and remarkably shorten the diffusion distance of ions, thus accelerating the transport of electrons and electrolyte ions. The XRD pattern of HT-MoS_2 is also shown (Fig. S3†) for comparison, where the sharp diffraction peaks indicate its higher crystallinity due to the longer hydrothermal process.

To gain further insight into the morphology and structure evolution process from the as-prepared intermediate precipitate to MW-MoS_2, (HR)TEM images were obtained and are shown in Fig. 2b–f. Well distributed homogeneous 2D layered particles comprising several monosheets with the size of about dozens of nanometers are observed for the intermediate precipitate (Fig. 2b and c). Additionally, no apparent diffraction ring is observed in the selected area electron diffraction (SAED) patterns of the intermediate precipitate (insert in Fig. 2b), which indicates its amorphous nature and is consistent with the XRD analysis. However, for MW-MoS_2, uniform small particles with sizes of about 20–30 nm are observed in the TEM images (Fig. 2d and e). The (100) lattice planes clearly observed in its HRTEM image (Fig. 2f) indicate the perfect crystallinity of the MoS_2 particles. Moreover, the (100) and (110) lattice planes, corresponding to perfect crystalline MoS_2 particles, are also clearly observed in the SAED patterns of MW-MoS_2 (inset in Fig. 2d), which are consistent with the XRD and (HR)TEM analyses.[26,33,38,39]

The N_2 adsorption–desorption isotherms and porosity distribution of MW-MoS_2 were examined to determine its textural characteristics. The typical type-IV isotherm (Fig. 3a) is observed for MW-MoS_2, and it possesses higher BET surface area of 96.9 m^2 g^{-1} than that ever reported for pure MoS_2,[26,28,33,39] which is almost five times that of HT-MoS_2 (21.9 m^2 g^{-1}) (Fig. S4†). This high specific surface area may provide more contact area between the electrode and electrolyte, which is beneficial for offering more active sites at the

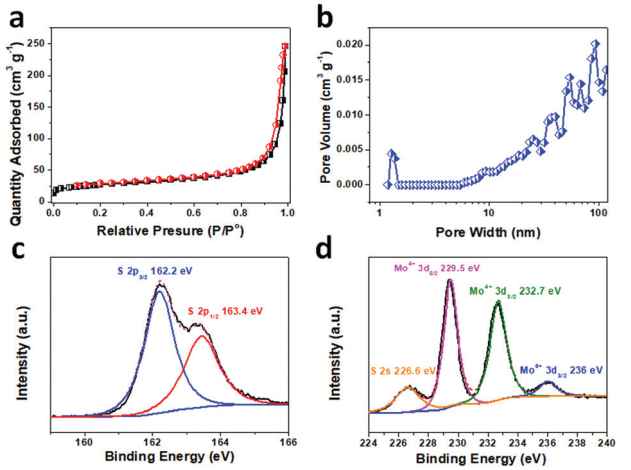

Fig. 3 (a) N_2 adsorption–desorption isotherms, (b) pore size distribution and (c) S 2p and (d) Mo 3d XPS spectra of MW-MoS_2.

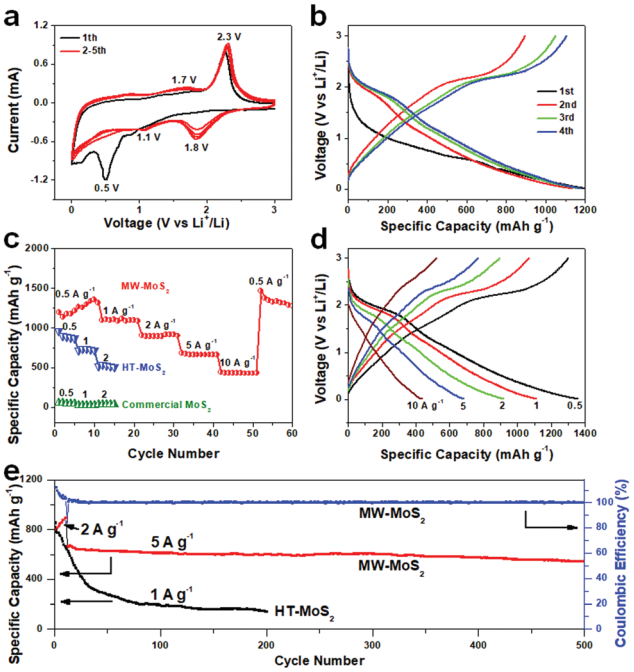

Fig. 4 First five (a) CV curves and (b) galvanostatic charge/discharge profiles of MW-MoS_2 at 0.5 A g^{-1} from the 1st to 10th cycles. (c) Rate capabilities of MW-MoS_2, HT-MoS_2 and the commercial MoS_2 at different current densities from 0.5 to 10 A g^{-1}. (d) Galvanostatic charge/discharge profiles of MW-MoS_2 at current densities ranging from 0.5 to 10 A g^{-1}. (e) Cyclic stabilities of MW-MoS_2 and HT-MoS_2.

interface between the solid and liquid. Also, the pore volume of MW-MoS_2 is 0.38 cm^3 g^{-1}, which is much larger than that of HT-MoS_2 (0.08 cm^3 g^{-1}). Moreover, the pore size of MW-MoS_2 (Fig. 3b) is mainly distributed in the range of meso/macropores, which is helpful for the transport of electrolyte ions and electrolyte storage. The large pore surface area and volume of the small-sized MoS_2 may also ease the volume expansion during the charging and discharging process.

S 2p and Mo 3d XPS were used to determine the phase of MW-MoS_2. As shown in Fig. 3c, there are two peaks of S 2p located at 162.2 eV and 163.4 eV, which correspond to the S $2p_{3/2}$ and S $2p_{1/2}$ orbitals of divalent sulfide ions (S^{2-}) in 2H-MoS_2.[21,24] The two major peaks located at 229.5 and 232.7 eV in the Mo 3d XPS spectrum (Fig. 3d) correspond to Mo $3d_{5/2}$ and $3d_{3/2}$, which are characteristic of Mo^{4+} in 2H-MoS_2. A small S 2s peak is located at 226.6 eV,[28,40,41] and the weak peak at 236 eV may be ascribed to the presence of Mo^{6+} $3d_{5/2}$ due to the surface oxidation of Mo.[29,42] Thus, MW-MoS_2 is a pure 2H-MoS_2 phase.

To evaluate the lithiation/dilithiation processes of the MW-MoS_2 electrode, CV tests were carried out at a scan rate of 0.2 mV s^{-1} over a potential window of 0.01–3.00 V (Fig. 4a). During the first discharging process, one dominant reduction peak located at 0.50 V was observed, which may be ascribed to the conversion reaction of Li_xMoS_2 into Li_2S and metallic Mo;[43–46] this peak disappeared in the following discharge curves. Two new reduction peaks at 1.8 and 1.1 V appeared, which may be ascribed to the formation of Li_2S and Li_xMoS_2 from the following reactions:[47] $2Li^+ + S + 2e \rightarrow Li_2S$ and $MoS_2 + xLi^+ + xe \rightarrow Li_xMoS_2$. In the anodic scans, two peaks are observed at 1.7 and 2.3 V. The weak and broad anodic peak at about 1.7 V can be assigned to the partial oxidation of Mo. The pronounced oxidation peak at 2.3 V indicates the formation of sulphur based on the reaction:[43] $Li_2S \rightarrow Li + S + 2e$. The curves almost overlapped in the following cycles, indicating that the small-sized electrode possesses high reversibility and cyclic stability in the electrochemical processes.[24] It should be stated that after the first cycle, the electrode material is mainly composed of sulfur, Mo, and few MoS_2 particles, instead of the initial amount of MoS_2, and this composition remains stable in the following cycles.[42]

Fig. 4b presents the galvanostatic discharge/charge profiles of MW-MoS_2 recorded for different cycles at a current density of 0.5 A g^{-1}. The evident plateaus at 1.7 and 2.3 V during the charging process and 1.8 V during the discharging process are consistent with the peaks in the CV curves. MW-MoS_2 delivered an initial capacity of 1199 mA h g^{-1} with a coulombic efficiency (CE) of 75%. The irreversible capacity may be due to the formation of an SEI film. A high specific capacity of 1355 mA h g^{-1} was obtained after 10 cycles at the low current density of 0.5 A g^{-1}, which is slightly larger than the initial capacity due to the activation effect.[48,49]

The rate capabilities of the MW-MoS_2 samples at current densities ranging from 0.5 to 10 A g^{-1} are given in Fig. 4c and the discharge curves at different current densities are shown in Fig. 4d. The initial plateau observed at about 1.8 V in the discharge curve at 0.5 A g^{-1} decreased stepwise (Fig. 4d) and the discharge capacity changed from 1355 to 438 mA h g^{-1} when the current density was gradually elevated from 0.5 to 10 A g^{-1} due to the rising polarization effect. To the best of our knowledge, the capacity data obtained is clearly superior to that of the reported pure MoS_2 LIB anodes[3,26,27,33,39,50–53]

Table 1 The rate capabilities and cyclic stabilities of the typical reported MoS_2 and MW-MoS_2

Electrode	Rate capability: Capacity (mA h g^{-1})/current density (A g^{-1})	Cycle stability: Capacity (mA h g^{-1})/current density (A g^{-1})/cycling number	Ref.
Hierarchical MoS_2 microspheres	353/1	672/0.1/50	3
MoS_2 tubes	600/1 500/5	839/0.1/50	26
N-Doped MoS_2	680/1 610/2	998/0.05/100	27
3D honeycomb-MoS_2	463/2	1025/0.1/50	33
Hierarchical MoS_2 microboxes	700/1	900/0.1/50	39
Inorganic fullerene-like MoS_2	680/1	1044/0.1/100	48
MoS_2 nanospheres	602/1	1095/0.1/100	49
MoS_2 nanoplates	950/1	910/1/50	50
Graphitized CNCs	150/0.8	335/0.1/400	53
Small-sized MW-MoS_2	1355/0.5 1111/1 683/5 438/10	544/5/500	This work

(Table 1). The excellent rate capability of our MW-MoS_2 may be due to its small particle size, which remarkably shortens the diffusion distance of ions and accelerates the transport efficiency of electrons and electrolyte ions; also, its large surface area is greatly beneficial for offering more active sites at the interface between the solid and liquid. Moreover, the large pore surface area and volume of the small-sized MoS_2 can ease the volume expansion during the charging and discharging process. The capacity can be still stabilized at about 1300 mA h g^{-1} when the current density returns to 0.5 A g^{-1}, which is 108.5% of the initial capacity caused by the activation of the electrode.[48,49] The rate capabilities of HT-MoS_2 and the commercial MoS_2 were also studied for comparison. The discharge capacities were 530/50, 340/27 and 136/32 mA h g^{-1} at current densities of 0.5, 1 and 2 A g^{-1} for the HT-MoS_2 and commercial MoS_2 electrodes, respectively, which demonstrate their lower capacities and fast capacity fading with an increase in current densities.

The cyclic stabilities of the MW-MoS_2 electrode were evaluated at the current density of 5 A g^{-1} with 10 cycles of activation at 2 A g^{-1} (Fig. 4e). The initial capacity of 664 mA h g^{-1} gradually changed to 544 mA h g^{-1} after 500 cycles with a capacity retention of ~82%, which corresponds to 0.037% capacity loss per cycle. In contrast, HT-MoS_2 only had a capacity of 142 mA h g^{-1} after 200 cycles at 1 A g^{-1}. It is very rare that pure-phase MoS_2 can still retain a high discharge capacity after numerous cycles at a high current density (Table 1), indicating the highly stable rate capability of MW-MoS_2.

Furthermore, EIS, XRD and (HR)TEM measurements were carried out for the above electrodes after 500 cycles at 5 A g^{-1} to gain insight into the discharge/charge processes and understand the nature of the high lithium storage characteristics in our unique MW-MoS_2. Fig. 5a shows the Nyquist plots of HT-MoS_2 before cycling and MW-MoS_2 before and after 500 cycles. Two parts comprising a semicircle in the high frequency region and an oblique inclined line in the low frequency region are observed in the Nyquist plots; the arcs are mainly caused by the charge-transfer reaction at the electrode/electrolyte interface.[54] During the charging–discharging process, the extraction and insertion of Li^+ ions and redox reactions of Mo ions occurred.[55,56] The Nyquist plots can be represented by the equivalent circuit (insert in Fig. 5a), where the intercept of the semicircle at the real axis reflects the resistance of electrolyte diffusion (R_s) and its diameter corresponds to the charge-transfer resistance (R_{ct}) Additionally, the oblique inclined line in the low-frequency region represents the Warburg-type resistance (Z_w), which is caused by ion diffusion in the electrode.[57,58] The R_{ct} value (68 Ω) of the as-synthesized MW-MoS_2 is much lower than that of HT-MoS_2 (195 Ω), and this value slightly increased to 84 Ω after cycling due to the high charge transfer resistance of the discharge products of $LiMoS_2$, Mo, S, and Li_2S as well as the residual MW-MoS_2. The Nyquist plot of MW-MoS_2 has a greater slope than that observed for HT-MoS_2 before cycling, suggesting that

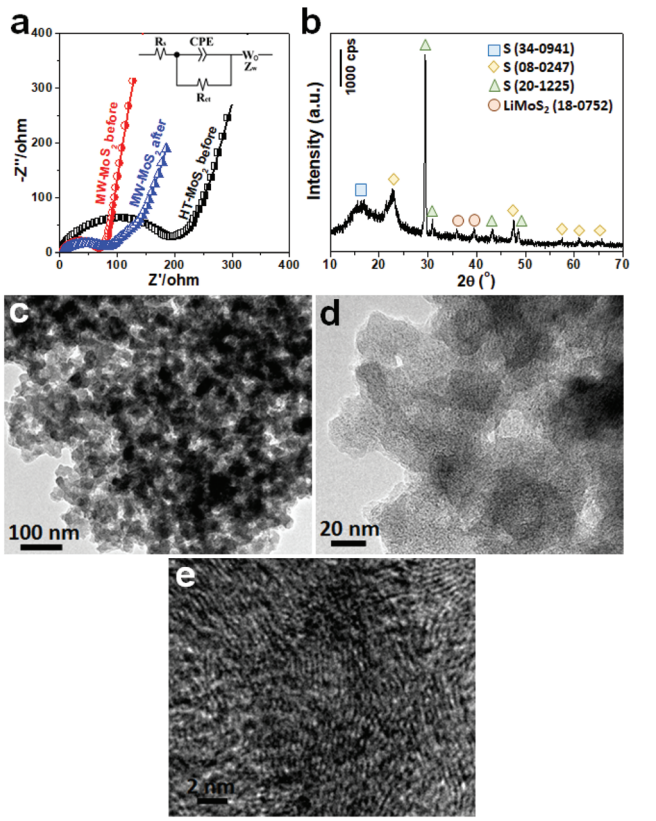

Fig. 5 (a) Nyquist plots of HT-MoS_2 before cycling and MW-MoS_2 before and after 500 cycles at 5 A g^{-1}. (b) XRD, (c, d) TEM and (e) HRTEM images of MW-MoS_2 after 500 cycles at 5 A g^{-1}. Inset in (a) is the equivalent circuit.

$MW\text{-}MoS_2$ has better ion diffusion capability in the electrode than $HT\text{-}MoS_2$. This is due to the large surface area of $MW\text{-}MoS_2$, which facilitates Li^+ ion insertion with a lower barrier; also, its smaller size significantly reduces the charge transfer resistance. These phenomena are consistent with the results of the cyclic and rate capability tests as well as the CV measurements.

The XRD (Fig. 5b) peaks observed at the 2θ values of 23.08, 47.83, 57.52, 61.12 and 65.75° can be unambiguously assigned to the (222), (515), (606), (3511) and (715) lattice planes of sulfur (PDF no. 08-0247), respectively, and the broad peak at about 16.25° can be assigned to the (200) lattice plane of sulfur (PDF no. 34-0941). Additionally, the peaks at 29.35, 30.88, 43.25 and 48.37° may be assigned to sulfur (PDF no. 20-1225), and the peaks at 36.04 and 39.31° may be assigned to the discharge product of $LiMoS_2$ (PDF no. 18-0752), as indicated by the CV analyses. No diffraction peaks of Li_2S or Mo were found in the XRD patterns, possibly due to their amorphous structures or low contents in the discharge products. The small-sized MoS_2 was still preserved after cycling according to the TEM image (Fig. 5c and d) and the (100) lattice planes can be clearly observed in the HRTEM image (Fig. 5e). These results indicate that the structure of the partial $MW\text{-}MoS_2$ electrode was hardly changed after cycling, demonstrating its high cyclic stability.

4. Conclusions

In summary, a novel solution-based microwave-assisted precursor pyrolysis method has been invented to prepare perfectly crystalline $2H\text{-}MoS_2$ with uniform particle sizes of 20–30 nm. The small-sized $MW\text{-}MoS_2$ nanoparticles exhibit a high surface area and large pore volume with a pore size distribution mainly in the meso/macropore scale, which are beneficial for electrolyte storage and low charge carrier conductive resistances. The large pore surface area and volume of the small-sized MoS_2 can ease the volume expansion during charging and discharging. As an LIB anode, the $MW\text{-}MoS_2$ electrode presented an unprecedented initial specific capacity, remarkably high cyclic stability and excellent rate capability. This study also highlights the universal solution-based microwave-assisted precursor pyrolysis strategy to synthesize small particle materials with large surface area and unique structures, which may lead to some particular advantages in various applications, particularly in the field of LIBs.

Conflicts of interest

There are no conflicts to declare.

Acknowledgements

This study was supported by National Basic Research Programs of China (973 Program, no. 2014CB931800 and 2011CB935700), Chinese National Science Foundation (no. 21571010 and U0734002), Chinese Aeronautic Project (no. 2013ZF51069) and 111 Project (no. B14009).

References

1 H. Jiang, Y. J. Hu, S. J. Guo, C. Y. Yan, P. S. Lee and C. Z. Li, *ACS Nano*, 2014, **8**, 6038–6046.
2 Y. X. Tang, Y. Y. Zhang, J. Y. Deng, J. Q. Wei, H. T. Tam, B. K. Chandran, Z. L. Dong, Z. Chen and X. D. Chen, *Adv. Mater.*, 2014, **26**, 6111–6118.
3 S. Ding, D. Zhang, J. S. Chen and X. W. Lou, *Nanoscale*, 2012, **4**, 95–98.
4 L. Lin, Z. Ji, M. Alcoutlabi and X. Zhang, *Energy Environ. Sci.*, 2011, **4**, 2682–2699.
5 M. H. Yu, S. B. Zhao, H. B. Feng, L. Hu, X. Y. Zhang, Y. X. Zeng, Y. X. Tong and X. H. Lu, *ACS Energy Lett.*, 2017, **8**, 1862–1868.
6 S. B. Wang, B. Y. Guan, L. Yu and X. W. Lou, *Adv. Mater.*, 2017, **29**, 1702724.
7 J. V. Laveda, V. Chandhok, C. A. Murray, G. W. Paterson and S. A. Corr, *Chem. Commun.*, 2016, **52**, 9028–9031.
8 X. Huang, Z. Zeng and H. Zhang, *Chem. Soc. Rev.*, 2013, **42**, 1934–1946.
9 J. Xiao, X. J. Wang, X. Q. Yang, S. D. Xun, G. Liu, P. K. Koech, J. Liu and J. P. Lemmon, *Adv. Funct. Mater.*, 2011, **21**, 2840–2846.
10 H. Y. Wang, H. Jiang, Y. J. Hu, N. Li, X. J. Zhao and C. Z. Li, *J. Mater. Chem. A*, 2017, **5**, 5383–5389.
11 H. M. Ji, C. Liu, T. Wang, J. Chen, Z. N. Mao, J. Zhao, W. H. Hou and G. Yang, *Small*, 2015, **11**, 6480–6490.
12 M. Chhowalla, H. S. Shin, G. Eda, L. J. Li, K. P. Loh and H. Zhang, *Nat. Chem.*, 2013, **5**, 263.
13 X. D. Duan, C. Wang, J. C. Shaw, R. Cheng, Y. Chen, H. L. Li, X. P. Wu, Y. Tang, Q. L. Zhang, A. L. Pan, J. H. Jiang, R. Q. Yu, Y. Huang and X. F. Duan, *Nat. Nanotechnol.*, 2014, **9**, 1024.
14 M. Y. Li, Y. M. Shi, C. C. Cheng, L. S. Lu, Y. C. Lin, H. L. Tang, M. L. Tsai, C. W. Chu, K. H. Wei, J. H. He, W. H. Chang, K. Suenaga and L. J. Li, *Science*, 2015, **349**, 524–528.
15 Q. Liu, X. L. Li, Q. He, A. Khalil, D. B. Liu, T. Xiang, X. J. Wu and L. Song, *Small*, 2015, **11**, 5556–5564.
16 S. S. Chou, D. B. Kaehr, J. Kim, B. M. Foley, D. M. De, P. E. Hopkins, J. Huang, C. J. Brinker and V. P. Dravid, *Angew. Chem., Int. Ed.*, 2013, **125**, 4254–4258.
17 W. Yin, L. Yan, J. Yu, G. Tian, L. Zhou, X. Zheng, X. Zhang, Y. Yong, J. Li, Z. Gu and Y. Zhao, *ACS Nano*, 2014, **8**, 6922–6933.
18 D. Voiry, M. Salehi, R. Silva, T. Fujita, M. W. Chen, T. Asefa, V. B. Shenoy and G. Eda, *Nano Lett.*, 2013, **13**, 6222–6227.
19 J. Yang, K. Wang, J. X. Zhu, C. Zhang and T. X. Liu, *ACS Appl. Mater. Interfaces*, 2016, **8**, 31702–31708.
20 Y. M. Chen, X. Y. Yu, Z. Li, U. Paik and X. W. Lou, *Sci. Adv.*, 2016, **2**, e1600021.

21 Z. Wan, J. Shao, J. Yun, H. Zheng, T. Gao, M. Shen, Q. Qu and H. Zheng, *Small*, 2014, **10**, 4975–4981.
22 X. Y. Yu, H. Hu, Y. Wang, H. Chen and X. W. Lou, *Angew. Chem., Int. Ed.*, 2015, **54**, 7395–7398.
23 S. K. Das, R. Mallavajula, N. Jayaprakash and L. A. Archer, *J. Mater. Chem.*, 2012, **22**, 12988–12992.
24 J. Wang, J. Liu, D. Chao, J. Yan, J. Lin and Z. X. Shen, *Adv. Mater.*, 2014, **26**, 7162–7169.
25 M. Wu, J. Zhan, K. Wu, Z. Li, L. Wang, B. Geng, L. Wang and D. Pan, *J. Mater. Chem. A*, 2017, **5**, 14061–14069.
26 P. Wang, H. Sun, Y. Ji, W. Li and X. Wang, *Adv. Mater.*, 2014, **26**, 964–969.
27 S. Qin, W. Lei, D. Liu and Y. Chen, *J. Mater. Chem. A*, 2016, **4**, 1440–1445.
28 S. Hu, W. Chen, J. Zhou, F. Yin, E. Uchaker, Q. F. Zhang and G. Z. Cao, *J. Mater. Chem. A*, 2014, **2**, 7862–7872.
29 W. S. V. Lee, E. Peng, T. A. J. Loh, X. L. Huang and J. M. Xue, *Nanoscale*, 2016, **8**, 8042–8047.
30 P. Gao, L. Wang, L. Chen, X. Jiang, J. Pinto and G. Yang, *Electrochim. Acta*, 2013, **100**, 125–132.
31 C. T. Hsieh, C. Y. Mo, Y. F. Chen and Y. J. Chung, *Electrochim. Acta*, 2013, **106**, 525–533.
32 G. Yang, H. Liu, H. Ji, Z. Chen and X. Jiang, *J. Power Sources*, 2010, **195**, 5374–5378.
33 J. W. Zhou, J. Qin, N. Q. Zhao, C. S. Shi, E. Z. Liu, F. He, J. J. Lia and C. N. He, *J. Mater. Chem. A*, 2016, **4**, 8734–8741.
34 S. Rajagopal, D. Nataraj, O. Y. Khyzhun, Y. Djaoued, J. Robichaud, K. Senthild and D. Mangalaraje, *CrystEngComm*, 2011, **13**, 2358–2368.
35 R. Matte, H. S. S. Gomathi, A. Manna, A. K. Late, D. J. Datta, R. Pati, S. K. Rao and C. N. R, *Angew. Chem., Int. Ed.*, 2010, **49**, 4059–4062.
36 L. Yang, S. Wang, J. Mao, J. Deng, Q. Gao, Y. Tang and O. G. Schmidt, *Adv. Mater.*, 2013, **25**, 1180–1184.
37 T. Yang, Y. Chen, B. Qu, L. Mei, D. Lei, H. Zhang, Q. Li and T. Wang, *Electrochim. Acta*, 2014, **115**, 165–169.
38 H. Li, C. Tsai, A. L. Koh, L. Cai, A. W. Contryman, A. H. Fragapane, J. Zhao, H. S. Han, H. C. Manoharan, F. Abild-Pedersen, J. K. Nørskov and X. Zheng, *Nat. Mater.*, 2016, **15**, 48.
39 L. Zhang, H. B. Wu, Y. Yan, X. Wang and X. W. Lou, *Energy Environ. Sci.*, 2014, **7**, 3302–3306.
40 T. H. Ning, Z. Liu, A. P. Hu, Q. L. Tang, B. B. Fan, S. Y. Zhang, W. N. Deng, K. K. Xiao and X. H. Chen, *J. Alloys Compd.*, 2018, **744**, 75–81.
41 A. Gigot, M. Fontana, M. Serrapede, M. Castellino, S. Bianco, M. Armandi, B. Bonelli, C. F. Pirri, E. Tresso and P. Rivolo, *ACS Appl. Mater. Interfaces*, 2016, **8**, 32842–32852.
42 Y. Q. Teng, H. L. Zhao, Z. J. Zhang, Z. L. Li, Q. Xia, Y. Zhang, L. N. Zhao, X. F. Du, Z. H. Du, P. P. Lv and K. Swierczek, *ACS Nano*, 2016, **10**, 8526–8535.
43 Y. Jing, E. O. Ortiz-Quiles, C. R. Cabrera, Z. Chen and Z. Zhou, *Electrochim. Acta*, 2014, **147**, 392–400.
44 Y. C. Liu, Y. P. Zhao, L. F. Jiao and J. Chen, *J. Mater. Chem. A*, 2014, **2**, 13109–13115.
45 Y. P. Tang, D. Q. Wu, Y. Y. Mai, H. Pan, J. Cao, C. Q. Yang, F. Zhang and X. L. Feng, *Nanoscale*, 2014, **6**, 14679–14685.
46 G. Huang, T. Chen, W. Chen, Z. Wang, K. Chang, L. Ma, F. Huang, D. Chen and J. Y. Lee, *Small*, 2013, **9**, 3693–3703.
47 T. Stephenson, Z. Li, B. Olsen and D. Mitlin, *Energy Environ. Sci.*, 2014, **7**, 209–231.
48 K. Chang, W. Chen, L. Ma, H. Li, H. Li, F. Huang, Z. Xu, Q. Zhang and J. Y. Lee, *J. Mater. Chem.*, 2011, **21**, 6251–6257.
49 Z. Hu, L. Wang, K. Zhang, J. Wang, F. Cheng, Z. Tao and J. Chen, *Angew. Chem., Int. Ed.*, 2014, **126**, 13008–13012.
50 X. Zuo, K. Chang, J. Zhao, Z. Xie, H. Tang, B. Li and Z. Chang, *J. Mater. Chem. A*, 2016, **4**, 51–58.
51 S. P. Zhang, B. V. R. Chowdari, Z. Y. Wen, J. Jin and J. H. Yang, *ACS Nano*, 2015, **9**, 12464–12472.
52 H. Hwang, H. Kim and J. Cho, *Nano Lett.*, 2011, **11**, 4826–4830.
53 L. Y. Wang, Z. J. Liu, Q. G. Guo, G. Z. Wang, J. H. Yang, P. Li, X. L. Wang and L. Liu, *Electrochim. Acta*, 2016, **199**, 204–209.
54 L. Gassa, H. Mishima, B. L. de Mishima and J. Vilche, *Electrochim. Acta*, 1997, **42**, 1717–1723.
55 M. H. Wu, J. Zhan, K. Wu, Z. Li, L. Wang, B. J. Geng, L. J. Wang and D. Y. Pan, *J. Mater. Chem. A*, 2017, **5**, 14061–14069.
56 Y. W. Wang, L. Yu and X. W. Lou, *Angew. Chem., Int. Ed.*, 2016, **55**, 7423–7426.
57 A. R. Park, D. Y. Son, J. S. Kim, J. Y. Lee, N. G. Park, J. H. Park, J. K. Lee and P. J. Yoo, *ACS Appl. Mater. Interfaces*, 2015, **7**, 18483–18490.
58 M. R. Busche, T. Drossel, T. Leichtweiss, D. A. Weber, M. Falk, M. Schneider, M. L. Reich, H. Sommer, P. Adelhelm and J. Janek, *Nat. Chem.*, 2016, **8**, 426.

